



Conformal SnO_x Heterojunction Coatings for Stabilized Photoelectrochemical Water Oxidation using Arrays of Silicon Microcones

Journal:	<i>Journal of Materials Chemistry A</i>
Manuscript ID	TA-ART-01-2020-001144.R1
Article Type:	Paper
Date Submitted by the Author:	01-Apr-2020
Complete List of Authors:	Moreno-Hernandez, Ivan; California Institute of Technology, Chemistry and Chemical Engineering Yalamanchili, Sisir; California Institute of Technology, Division of Materials Science; California Institute of Technology, Division of Materials Science Fu, Harold; California Institute of Technology, Chemistry and Chemical Engineering Atwater, Jr., Harry; California Institute of Technology, Brunschwig, Bruce; California Institute of Technology , Beckman Institute Lewis, Nathan; California Institute of Technology, Chemistry and Chemical Engineering

Conformal SnO_x Heterojunction Coatings for Stabilized Photoelectrochemical Water Oxidation using Arrays of Silicon Microcones

Ivan A. Moreno-Hernandez¹, Sisir Yalamanchili³, Harold J. Fu¹, Harry A. Atwater^{3,4}, Bruce S. Brunshwig², Nathan S. Lewis^{1,2,4}

¹Division of Chemistry and Chemical Engineering, 127-72, California Institute of Technology, Pasadena, CA 91125, USA

²Beckman Institute Molecular Materials Research Center, California Institute of Technology, Pasadena, CA 91125, USA

³Division of Engineering and Applied Sciences, California Institute of Technology, Pasadena, CA 91125

⁴Kavli Nanoscience Institute, California Institute of Technology, Pasadena, CA 91125, USA

*Correspondence to: nslewis@caltech.edu

Abstract:

The efficiency of photoelectrodes towards fuel-forming reactions is strongly affected by surface-based charge recombination, charge-transfer losses, and parasitic light absorption by electrocatalysts. We report a protective tin oxide (SnO_x) layer formed by atomic-layer deposition that limits surface recombination at n-Si/ SnO_x heterojunctions and produces ~ 620 mV of photovoltage on planar n-Si photoanodes. The SnO_x layer can be deposited conformally on high aspect-ratio three-dimensional structures such as Si microcone arrays. Atomic-level control of the SnO_x thickness enabled highly conductive contacts to electrolytes, allowing the direct electrodeposition of NiFeOOH , CoO_x , and IrO_x electrocatalysts for photoelectrochemical water oxidation with minimal parasitic absorption losses. SnO_x -coated n-Si microcone arrays coupled to electrodeposited catalysts exhibited photocurrent densities of ~ 42 mA cm^{-2} and a photovoltage of ~ 490 mV under 100 mW cm^{-2} of simulated solar illumination. The SnO_x layer can be integrated with amorphous TiO_2 to form a protective $\text{SnO}_x/\text{TiO}_2$ bilayer that exhibits the beneficial properties of both materials. Photoanodes coated with $\text{SnO}_x/\text{TiO}_2$ exhibited a similar photovoltage to that of SnO_x -coated photoanodes, and showed > 480 h of stable photocurrent for planar photoelectrodes and > 140 h of stable photocurrent for n-Si microcone arrays under continuous simulated solar illumination in alkaline electrolytes.

Introduction

High aspect-ratio structures are promising for photoelectrochemical water splitting due to the minimal use of semiconducting material, the potential to obtain high efficiencies with defective materials by decoupling of the paths of light absorption and charge-carrier collection, and the ability to use high catalyst loadings while minimizing parasitic light absorption.¹⁻³ Silicon microwire array photoanodes generally utilize diffused p-n junctions to obtain the large photovoltages necessary to drive electrochemical reactions.^{1, 4, 5} Si microcone (μcn) arrays have been proposed as an alternative to Si microwire arrays, because microcones can maximize light absorption via enhanced coupling of broadband light to available waveguide modes and thus increase device efficiencies while maintaining the advantages associated with the microwire array morphology.^{6, 7} However, high aspect-ratio structures such as microwires and microcones introduce additional challenges, such as non-standard surface terminations as well as additional surface area that can increase surface recombination and limit device performance.

The oxidation of water to $\text{O}_2(\text{g})$ is a key reaction in photoelectrochemical systems that produce sustainable fuels.⁸ Without a protective coating, most efficient semiconductors passivate or corrode while performing solar-driven $\text{O}_2(\text{g})$ evolution in contact with highly acidic or alkaline aqueous electrolytes.^{9, 10} Optimal metal oxide protective coatings provide a conductive pathway to catalytically active sites and can moreover provide additional functionality such as anti-reflective interfaces, intrinsic catalytic activity without additional catalyst deposition, and an appropriate work function to form a high photovoltage semiconductor/metal-oxide heterojunction.^{9, 10} TiO_2 , Ni, NiO_x , CoO_x , NiCoO_x , MnO_x , ITO, SiO_2 , and SnO_x have been used to protect photoanodes in strongly alkaline electrolytes, and materials such as polymers, TiO_2 , Ir/IrO_x , and SnO_x have been used as protection layers in strongly acidic electrolytes.¹¹⁻²⁵

SnO_x can act as a protective heterojunction in strongly alkaline or acidic electrolytes, providing 620 mV of photovoltage on planar n-Si photoanodes with a solar-to- $\text{O}_2(\text{g})$ ideal regenerative cell photoelectrode efficiency, η_{IRC} , of 3.7-4.0%.^{12, 26} Herein we report the growth of conformal SnO_x layers by atomic-layer deposition as well as use of such films as heterojunctions, protective layers, and electrocatalyst integration layers on both planar Si and Si microcone array electrodes. The work presented herein addresses several challenges in the development of protective heterojunctions that have not been addressed in previous work focused on planar substrates, such as the formation of a high photovoltage heterojunction on microstructured substrates and integration of oxygen-evolving electrocatalysts with minimal parasitic light absorption. We demonstrate that SnO_x produces a low interface recombination velocity on planar and microcone array substrates, indicating that protective heterojunctions can be applied to microstructured substrates that are relevant to integrated photoelectrochemical devices, without substantial increases in surface recombination. Additionally, the thin SnO_x layers act as electrocatalyst integration layers that allow the direct electrodeposition of water oxidation catalysts, which enables enhanced loading of catalysts with minimal optical losses onto Si microcone arrays. The SnO_x layers can also be readily integrated with previously developed protective coatings to construct bilayers that exhibit the beneficial properties of both films. The $\text{SnO}_x/\text{TiO}_2$ bilayer allows the construction of photoanodes based on Si microcone arrays that exhibit a photovoltage of ~ 490 mV and a photocurrent density of ~ 34 mA cm^{-2} under sustained water oxidation conditions.

Results

1. Chemical Composition, Structure and Stability of ALD SnO_x Films on Planar Si(100)

Conformal coatings of SnO_x were deposited by atomic-layer deposition (ALD) at > 200 °C using tetrakis-dimethylamine tin and ozone (details in Supplementary Information) on oxidized planar Si(100) wafers.²⁷ Microwave conductivity decay measurements indicated that intrinsically doped, 300 μm thick, double-side-polished, float-zone Si(100) wafers (with a bulk lifetime > 1.5 ms) that were coated with a chemically formed SiO_x layer and 100 ALD cycles of SnO_x at 210 °C had a charge-carrier lifetime of 37 ± 1 μs, implying a surface recombination velocity of ~ 400 cm s⁻¹.

In contact with Fe(CN)₆^{3-/4-}(aq), n-Si(100)/SiO_x/SnO_x electrodes with SnO_x deposited at 210-220 °C (Figure S1) exhibited photovoltages of 620 ± 2 mV under 100 mW cm⁻² of simulated solar illumination, with barrier heights of 1.01 ± 0.02 eV as determined by differential capacitance vs. potential measurements (Figure S1c). Photoelectrodes without an intentionally formed SiO_x layer exhibited photovoltages of ~ 425 mV (Figure S1a). Between 15 – 60 mA cm⁻² of light-limited photocurrent density, the n-Si(100)/SiO_x/SnO_x photoanodes exhibited a diode quality factor of $n = 1.07$ and a saturation current density of $J_0 = 1.3 \times 10^{-11}$ A cm⁻², whereas between 0.3 - 8 mA cm⁻² of light-limited photocurrent density, n-Si(100)/SiO_x/SnO_x photoanodes exhibited $n = 2.44$ and $J_0 = 8.1 \times 10^{-7}$ A cm⁻² (Figure S1d).

Transmission-electron microscopy (TEM) data on the n-Si(100)/SiO_x/SnO_x interface indicated that the SiO_x layer was 1.4 ± 0.1 nm thick and amorphous (Figure 1a). The SnO_x films deposited with 850 ALD cycles were 90 ± 3 nm thick, corresponding to a growth rate of 1.06 ± 0.04 Å cycle⁻¹ (Figure 1b). Dark-field imaging and high-resolution TEM images of the SnO_x layer indicated that the SnO_x film transitioned from amorphous to crystalline after ~ 18 nm of growth, and was terminated at the surface by polycrystalline SnO₂ (Figure 1a, S2). X-ray diffraction and

electron diffraction data indicated that the SnO_x layer contained nanocrystals of SnO_2 (Figure S2b, S3).

The electrochemical stability of the ALD SnO_x was determined by measuring the concentration of dissolved Sn species produced in 1.0 M KOH(aq) or 1.0 M H_2SO_4 (aq) using a $\text{p}^+\text{-Si}(100)/\text{SiO}_x/\text{SnO}_x$ anode held at 1.53 V vs. the reversible hydrogen electrode, RHE (Figure S4). A $\text{p}^+\text{-Si}$ substrate was used to control the electrochemical potential at the surface of the SnO_x film. For photoelectrodes constructed with an n-Si substrate, the potential at the surface is a combination of the photovoltage generated under illumination and the potential applied by the potentiostat. Prior to electrochemical testing, $\sim 3\text{-}12 \mu\text{g L}^{-1}$ of Sn was observed in the electrolyte, indicating an equivalent initial dissolved SnO_2 thickness of $3 \pm 1 \text{ nm}$ and $8 \pm 2 \text{ nm}$ in 1.0 M KOH(aq) and 1.0 M H_2SO_4 (aq), respectively. During operation of $\text{p}^+\text{-Si}/\text{SiO}_x/\text{SnO}_x$ anodes, the concentration of Sn in the electrolyte initially decreased, possibly due to deposition of Sn impurities in the electrolyte onto the SnO_x surface, then increased over the first 22 h. Subsequently, SnO_x exhibited a dissolution rate of $\sim 0.040 \text{ nm h}^{-1}$ in 1.0 M KOH(aq) and $\sim 0.028 \text{ nm h}^{-1}$ in 1.0 M H_2SO_4 (aq), implying $> 1,000 \text{ h}$ of continuous operation at anode potentials of 1.53 V vs. RHE would be needed to produce a 50% loss of a 90 nm thick SnO_x film.

2. *Optical and Electronic Properties of SnO_x Films on Si*

The band-edge positions, work function, and chemical properties of the ALD SnO_x film were determined using X-ray photoelectron spectroscopy (XPS). Some properties were determined with ALD SnO_x films grown on quartz to remove the effect of Fermi-level equilibration between the n-Si substrate and the SnO_x film (Figure 2a, 2b, 3). After correction for the relative sensitivity factors of Sn and O, integration of the Sn 3d and O 1s signals indicated that

the surface stoichiometry of the SnO_x film was $1:1.47 \pm 0.02$ Sn:O (Figure 2). The Sn 3d XP spectra exhibited a Sn $3d_{5/2}$ peak at a binding energy of 486.7 ± 0.1 eV, whereas the O 1s spectra exhibited an asymmetric O 1s peak with a binding energy of 530.5 ± 0.1 eV. The binding energy ranges reported for the Sn 3d peaks of SnO and SnO_2 overlap, but could adequately be described by a single contribution assigned to SnO_2 .^{28, 29}

n-Si(100)/ SiO_x / SnO_x samples prepared with 50 ALD cycles exhibited an elemental Si $2p_{3/2}$ peak at a binding energy of 98.7 ± 0.1 eV (Figure 2c). The position of the Si $2p_{3/2}$ peak, at ~ 0.2 eV lower than the elemental binding energy of Si on n-Si(100)/ SiO_x electrodes that had nominally the same doping density as the n-Si(100)/ SiO_x / SnO_x samples, is consistent with an increase in band bending in the n-Si(100)/ SiO_x / SnO_x relative to n-Si/ SiO_x .³⁰ The $2p_{3/2}$ binding-energy peak separation between elemental Si and silicon oxide was 4.1 ± 0.1 eV in n-Si(100)/ SiO_x but was 2.9 ± 0.1 eV in n-Si(100)/ SiO_x / SnO_x (Figure 2c). The $2p_{3/2}$ peak separation of Si and SiO_x is typically ~ 3.8 eV. Decreases in this separation are consistent with band bending within the SiO_x and/or changes in the chemical composition of the SiO_x layer due to the ALD process step.³⁰

UV-Vis spectroscopy indicated that the optical band gap of the ALD SnO_x was 4.2 eV by (Figure 3a). Secondary-electron measurements of n-Si(100)/ SiO_x / SnO_x samples prepared using 850 ALD cycles of SnO_x indicated that the Fermi level was $> 4.7 \pm 0.1$ eV below the vacuum energy (Figure 3b). The valence band was 3.2 ± 0.1 eV below the Fermi level, and a defect band was observed at the Fermi level (Figure 3c). Hence, the conduction-band edge and valence-band edge of SnO_x are $3.5 \text{ eV} \pm 0.1 \text{ eV}$ and $7.7 \pm 0.1 \text{ eV}$, respectively, below the vacuum energy. n-Si(100)/ SiO_x / SnO_x samples that had an ~ 90 nm thick SnO_x layer exhibited an average reflectance of 9.9% over the 400 – 1000 nm wavelength range, as compared to 35.3 % for a n-Si(100)/ SiO_x device (Figure S5).

3. *Electrochemical Properties of SnO_x/Electrolyte Interfaces*

Figure S6 demonstrates the effect of SnO_x film thickness on the electrochemical properties of Si (photo)electrodes. As shown in Figure 1, SnO_x films deposited with 850 ALD cycles transition from amorphous to crystalline at ~ 18 nm of growth, which corresponds to 170 cycles of deposition from the measured growth rate. Samples prepared with 100 cycles or 850 cycles of SnO_x were studied to determine the effect of crystalline SnO_x on the electrochemical properties of the Si (photo)electrodes (Figure S6). Capacitance-voltage measurements of p⁺-Si(100)/SiO_x anodes with 850 cycles of SnO_x indicated that the ALD SnO_x film was n-type with a dopant concentration of $1.1 \times 10^{19} \text{ cm}^{-3}$. In contact with Fe(CN)₆^{3-/4-}(aq) in the absence of illumination, p⁺-Si(100)/SiO_x/SnO_x junctions exhibited a built-in voltage of $0.72 \pm 0.01 \text{ V}$ (Figure S6c). In contact with Fe(CN)₆^{3-/4-}(aq) under 100 mW cm^{-2} of simulated solar illumination, the fill factor of n-Si(100)/SiO_x/SnO_x electrodes decreased when > 100 ALD cycles of SnO_x deposition were used (Figure S6a). Four-point probe measurements indicated that the SnO_x films prepared at 210 °C had a resistivity of $2.3 \times 10^{-5} \Omega \text{ m}$, which would lead to a voltage drop of 2.3 nV at 100 mA cm^{-2} for 100 nm thick films. Compared to photoanodes without a Pt overlayer, photoanodes coated with 850 SnO_x ALD cycles exhibited an improved fill factor in contact with Fe(CN)₆^{3-/4-}(aq) when ~ 2 nm of Pt was sputtered onto the SnO_x surface (Figure S6b). Sputter deposition of a Pt overlayer on p⁺-Si(100)/SiO_x/SnO_x resulted in no observable n-type behavior in the capacitance-voltage measurements, indicating minimal band bending at the SnO_x/electrolyte surface (Figure S6d).

4. *Behavior of n-Si(100)/SnO_x Photoanodes Coated with Electrodeposited Catalysts*

Electrocatalysts for the oxygen-evolution reaction (OER) were deposited onto n-Si(100)/SiO_x/SnO_x photoanodes prepared using 100 ALD cycles of SnO_x (details in

Supplementary Information). Table S1 summarizes the photoelectrochemical behavior of the n-Si photoelectrodes studied herein. Nickel-iron oxyhydroxide (NiFeOOH), cobalt oxide (CoO_x) and iridium oxide (IrO_x) provided representative OER catalysts that could be electrodeposited and subsequently used for the OER in either 1.0 M KOH(aq) or 1.0 M H₂SO₄(aq).^{31, 32} Figure S7 shows the effect of NiFeOOH, CoO_x, and IrO_x catalyst loading on the photoelectrochemical behavior of n-Si(100)/SiO_x/SnO_x anodes in contact with 1.0 M KOH(aq) or 1.0 M H₂SO₄(aq). Figure S8 shows scanning-electron microscopy images of the catalysts electrodeposited on n-Si(100)/SiO_x substrates coated with 100 ALD cycles of SnO_x.

In contact with 1.0 M KOH(aq), the ideal regenerative cell solar-to-O₂(g) efficiency, η_{IRC} ,²⁶ was 3.5% for n-Si(100)/SiO_x/SnO_x photoanodes coated with 5 mC cm⁻² of electrodeposited NiFeOOH (Figure 4a). The n-Si(100)/SiO_x/SnO_x electrodes were coated with 1-2 μm long particles of electrodeposited NiFeOOH dispersed onto the electrode surface (Figure S8a, b). Further increases in NiFeOOH catalyst loading decreased the photocurrent density as well as the fill factor of the photoanodes (Figure S7a). 5 mC cm⁻² of photoanodically deposited CoO_x (Figure S8c) yielded $\eta_{\text{IRC}} = 2.6\%$ for n-Si/SiO_x/SnO_x photoanodes in contact with 1.0 M KOH(aq) (Figure 4a). Further increases in CoO_x loading led to more negative onset potentials for the OER but decreased the light-limited photocurrent density. Excessive CoO_x deposition decreased the light-limited photocurrent density as well as the fill factor (Figure S7b) of the resulting photoanodes. n-Si(100)/SiO_x/SnO_x photoanodes coated with electrodeposited IrO_x using 4 cyclic voltammetry scans under illumination in an Ir electrochemical deposition solution produced 50-500 nm long IrO_x nanoparticles and a wrinkled IrO_x film on the electrode surface (Figure S8d), and exhibited $\eta_{\text{IRC}} = 3.1\%$ in contact with 1.0 M H₂SO₄(aq) (Figure 4a). Further increases in IrO_x electrodeposition decreased the light-limited photocurrent density (Figure S7c).

Figure S9 shows high-resolution XPS data of n-Si(100)/SiO_x photoelectrodes coated with 100 ALD cycles of SnO_x and electrodeposited catalysts after short-term operation. The SnO_x film was not markedly altered after electrochemical deposition of the water oxidation catalysts, as indicated by the Sn 3d spectra of the SnO_x films (Figure S9a). The Ni 2p spectra of n-Si(100)/SiO_x/SnO_x electrodes coated with electrodeposited NiFeOOH are indicative of the presence of nickel hydroxide species (Figure S9b), consistent with previous reports of electrodeposited NiFeOOH catalysts and the reversible hydroxide/oxyhydroxide redox process at potentials relevant to the OER.³³ X-ray photoelectron spectra in the Fe 2p region could not be used to determine the oxidation state of Fe due to overlap with the Sn 3p signal. The percentage of the XPS signal attributed to SnO_x, Sn/(Sn+Ni), was 92 ± 1%, consistent with the surface coverage observed by scanning-electron microscopy (Figure S8b, S9). The Co 2p peaks of the electrodeposited CoO_x catalyst indicated the presence of oxidized Co species, consistent with contributions from Co₃O₄ and Co(OH)₂ (Figure S9c). The surface coverage of CoO_x was 98.4 ± 0.3%, as indicated by the Sn 3d and Co 2p signal fractions corrected by relative sensitivity factors (Figure 9a, c). The Ir 4f spectra had an asymmetric doublet with a peak separation of 2.98 eV and an Ir 4f_{7/2} binding energy of 62.5 ± 0.1 eV, consistent with the X-ray photoelectron spectra of hydrated IrO_x species (Figure S9d).³⁴ Sn could not be detected with XPS on IrO_x-coated electrodes, indicating coverage of the surface with the photoelectrodeposited catalyst (Figure S8, S9). Only Sn, O, and adventitious C were detected with XPS on the SnO_x surface prior to electrochemical deposition of catalyst films (Figure S9e). In Figure S8a, the SnO_x-coated Si substrate appears with minimal contrast due to the flat surface, whereas the IrO_x-coated electrodes appear to be coated by a wrinkled IrO_x film with dispersed IrO_x particles.

5. Behavior of Si Microcone Array Photoanodes Coated with SnO_x

Figure S10 shows the photoelectrochemical behavior of n-Si microcone (μcn) arrays that had been chemically oxidized to form a conformal SiO_x layer and then coated with 100 ALD cycles of SnO_x (n-Si(μcn)/ SiO_x / SnO_x). In contact with $\text{Fe}(\text{CN})_6^{3-/4-}(\text{aq})$ under 100 mW cm^{-2} of simulated solar illumination, the n-Si(μcn)/ SiO_x / SnO_x anodes exhibited a photovoltage of $\sim 490 \text{ mV}$, which was comparable to the photovoltage exhibited by n-Si(μcn) array electrodes that contained a diffused np⁺ junction (Figure S10a).

Water oxidation electrocatalysts (NiFeOOH , CoO_x , or IrO_x) were electrochemically or photoelectrochemically deposited on n-Si(μcn)/ SiO_x / SnO_x using similar conditions to those used to prepare planar n-Si(100) photoanodes. A larger deposition cathodic current density (-10 mA cm^{-2} instead of -1 mA cm^{-2}) was required to deposit NiFeOOH on n-Si (μcn) samples compared to planar n-Si(100) photoanodes. Figure S10 shows the effect of catalyst loading on the photoelectrochemical behavior of n-Si(μcn)/ SiO_x / SnO_x . An increase in catalyst loading generally led to an improvement in the onset potential observed for water oxidation until the optimal catalyst loading level (10 mC cm^{-2} , 10 mC cm^{-2} , and 4 CVs for NiFeOOH , CoO_x , and IrO_x , respectively) was obtained (Figure S10). Catalyst loadings beyond the optimal level led to a decrease in the light-limited photocurrent density, with the onset potential for water oxidation showing a negligible decrease for CoO_x and a substantial increase for NiFeOOH and IrO_x (Figure S10) as the catalyst loading increased. Scanning-electron microscopy images of n-Si(μcn) samples coated with 100 ALD cycles of SnO_x and optimal catalyst loadings indicated that compared to cathodic depositions (NiFeOOH), photoanodic depositions (CoO_x , IrO_x) led to preferential catalyst deposition on the tips of the microcones (Figure S11).

Figure 4b shows the photoelectrochemical behavior under 100 mW cm^{-2} of simulated solar illumination of n-Si(μcn)/ SiO_x / SnO_x photoanodes with optimal NiFeOOH , CoO_x , and IrO_x

loadings in contact with 1.0 M KOH(aq) or 1.0 M H₂SO₄(aq). The photoanodes coated with NiFeOOH or CoO_x exhibited an overpotential, $\eta = -186$ mV or $\eta = -167$ mV, respectively, at 1 mA cm⁻² in 1.0 M KOH(aq). n-Si(μ cn)/SiO_x/SnO_x photoanodes coated with IrO_x exhibited $\eta = -147$ mV at 1 mA cm⁻² in 1.0 M H₂SO₄(aq). The light-limited photocurrent density for n-Si(μ cn)/SiO_x/SnO_x anodes coated with NiFeOOH, CoO_x, or IrO_x was 41.2, 41.0, and 42.1 mA cm⁻² at 1.63 V vs. RHE, respectively, as compared to the theoretical value of 43.3 mA cm⁻² expected for unity external quantum yield for all photons in the 100 mW cm⁻² Air Mass 1.5G solar spectrum having energies greater than the 1.12 eV band gap energy of Si.³⁵ Under 100 mW cm⁻² of simulated solar illumination, n-Si(μ cn)/SiO_x/SnO_x electrodes coated with NiFeOOH, CoO_x, or IrO_x exhibited $\eta_{\text{IRC}} = 1.3\%$, 0.9% , and 1.0% , respectively. Silicon photoanodes coated with SnO_x/Ni exhibited a faradaic efficiency of at least 97.7% (Figure 4c). A sputtered Ni catalyst was used for faradaic efficiency measurements to produce a more uniform electrocatalyst coating on ~ 1 cm² photoelectrodes compared to the studied electrodeposition methods, which were optimized for ~ 0.1 cm² photoelectrodes.

Conformal coatings of amorphous TiO₂ were deposited on n-Si(μ cn)/SiO_x/SnO_x as well as on n-Si/SiO_x/SnO_x, to improve the stability of the photoanodes in 1.0 M KOH(aq).¹¹ Electrodes consisting of n-Si(100)/SiO_x/SnO_x/TiO₂ with 3.5 nm of Ni exhibited photovoltages of ~ 602 mV in contact with Fe(CN)₆^{3-/4-}(aq) under 100 mW cm⁻² of simulated solar illumination, whereas n-Si(μ cn)/SiO_x/SnO_x/TiO₂ photoanodes exhibited photovoltages of ~ 490 mV (Figure S12a). Planar photoanodes with a layer of SnO_x/TiO₂ and 3.5 nm Ni initially exhibited $\eta_{\text{IRC}} = 3.5\%$, with $\eta_{\text{IRC}} = 3.4\%$ after 50 h of operation under 100 mW cm⁻² of illumination in 1.0 M KOH(aq) (Figure 6a).

Figure S12b summarizes the band energetics of n-Si, SnO_x, and TiO₂ based on the data collected herein as well as previous results for amorphous TiO₂.³⁰

Planar n-Si photoelectrodes coated with SnO_x/TiO₂ and 3.5 nm of Ni exhibited a stable photocurrent in 1.0 M KOH(aq) for > 480 h (Figure 6b), whereas n-Si(μcn)/SiO_x/SnO_x/TiO₂ photoanodes with the same loading of Ni did not exhibit stable photoelectrochemical behavior in 1.0 M KOH(aq). The instability might be due to the same loading of Ni being deposited over a substantially higher surface area, resulting in thinner Ni coatings. The Ni coatings could gradually convert to Ni(OH)₂/NiOOH during electrochemical operation, leading to the loss of an ohmic Ni metal interface between TiO₂ and the active oxyhydroxide water oxidation electrocatalyst. Cyclic voltammograms of n-Si/SiO_x/SnO_x/TiO₂ photoanodes revealed a decrease in the fill factor after extended operation. This decrease coincided with an increase in the charge associated with the Ni(OH)₂/NiOOH redox peak (Figure 6a, S12c). Integration of the redox Ni(OH)₂/NiOOH reduction peak indicated that at initial operation, ~ 9% (0.5 mC cm⁻²) of the 3.5 nm Ni film was electrochemically active as Ni(OH)₂/NiOOH, and after 480 h ~ 100% (5.4 mC cm⁻²) of the Ni film as Ni(OH)₂/NiOOH. n-Si(μcn)/SiO_x/SnO_x/TiO₂ photoanodes with an Ni loading equivalent to 7 nm exhibited photovoltages of ~ 490 mV in contact with Fe(CN)₆^{3-/4-}(aq) under 100 mW cm⁻² of illumination (Figure S12a). The n-Si(μcn)/SiO_x/SnO_x/TiO₂ photoanodes with 7 nm Ni initially showed η_{IRC} ~ 0.5% with the efficiency increasing to η_{IRC} ~ 1.2% after 50 h, and exhibited a stable photocurrent for > 140 h of continuous operation (Figure 6c,d). Although some variability was observed in the photocurrent during the first 20 h of operation of n-Si(μcn)/SiO_x/SnO_x/TiO₂ photoanodes, cyclic voltammetry indicated a similar light-limiting photocurrent at 0 h and 70 h of operation (Figure 6c). The variability could be due to bubble detachment or changes in the Ni overlayer during continuous operation. The light intensity was re-calibrated at 120 h, and the n-

Si(μcn)/SiO_x/SnO_x/TiO₂ photoanode exhibited a steady photocurrent density of $\sim 34.5 \text{ mA cm}^{-2}$ from 125-135 h of operation. The cathodic peak of the Ni(OH)₂/NiOOH redox couple on n-Si(μcn)/SiO_x/SnO_x/TiO₂ photoanodes indicated that $\sim 17\%$ of the Ni was electrochemically active as Ni(OH)₂/NiOOH initially, and after 130 h $\sim 67\%$ of the Ni metal was converted to Ni(OH)₂/NiOOH (Figure S12c).

Discussion

In this work, various modifications to SnO_x-coated Si photoelectrodes were investigated, and their effect on the optoelectronic and electrochemical properties of the resulting photoelectrodes were determined. SnO_x films that are $\sim 11 \text{ nm}$ thick have an amorphous structure and can readily perform one-electron electrochemical reactions, whereas $\sim 90 \text{ nm}$ thick SnO_x films are terminated with polycrystalline SnO_x and exhibit slow charge-transfer kinetics (Figure 1, S6). The difference in the electrochemical kinetics is attributed to unfavorable band bending at the SnO_x/electrolyte interface that inhibits charge transfer (Figure S6). Thin SnO_x films allow the electrochemical deposition of electrocatalysts such as CoO_x, NiFeOOH, and IrO_x. Although IrO_x is the only catalyst studied that can operate in acidic electrolyte, both CoO_x and NiFeOOH operate in alkaline electrolytes. NiFeOOH is more active than CoO_x for water oxidation, as indicated by the improved onset potential on photoelectrodes (Figure 4). However, CoO_x can be deposited using anodic current, allowing the optoelectronic properties of Si microcone arrays to direct the deposition of CoO_x (Figure S11). Although the SnO_x films act as protective heterojunctions, the dissolution studies indicate a finite, non-zero rate of corrosion (Figure S4). Protective TiO₂ films were deposited on the surface to mitigate the slow but non-zero dissolution of the SnO_x film. The charge-transfer properties of the TiO₂ surface prevent direct electrodeposition of the catalysts studied herein, so a sputter-deposited Ni pre-catalyst was

used instead of electrodeposited catalysts.¹¹ In the subsequent sections, the effect of each particular modification is discussed in detail.

1. *Properties of Atomic Layer Deposited SnO_x Coatings on Si*

The conductivity through the SnO_x film is dependent on the degree of band-bending at the SnO_x/electrolyte interface. SnO_x films that were 90 nm thick exhibited slow charge-transfer kinetics to Fe(CN)₆^{3-/4-}(aq) (Figure S6a). Deposition of a thin metal film on SnO_x substantially improved the charge transfer kinetics to Fe(CN)₆^{3-/4-}(aq) and decreased the effective thickness of the SnO_x film (Figure S6b). The resistivity of the SnO_x film is $2.3 \times 10^{-5} \Omega \text{ m}$, which would lead to a voltage drop of $< 2.3 \text{ nV}$ at 100 mA cm^{-2} for $< 100 \text{ nm}$ thick films. This indicates that bulk conductivity cannot explain the slow interfacial charge-transfer kinetics to Fe(CN)₆^{3-/4-}(aq) for 90 nm thick films.

Impedance measurements indicated that SnO_x exhibited a barrier height of $V_b = 0.72 \text{ eV}$ in contact with Fe(CN)₆^{3-/4-}(aq), consistent with the slow interfacial charge transfer between SnO_x and Fe(CN)₆^{3-/4-}(aq) (Figure S6c). Deposition of a thin film of Pt on the surface of SnO_x led to negligible band-bending (Figure S6d). The amorphous-to-crystalline transition observed with transmission-electron microscopy coupled with the electrochemical data in Fe(CN)₆^{3-/4-}(aq) suggest that the amorphous SnO_x layer is not sensitive to band bending at the surface/electrolyte interface, whereas the conductivity through the polycrystalline SnO_x layer is substantially affected by band bending at the surface/electrolyte interface.

2. *Integration of Electrocatalysts with ALD SnO_x Films*

The high conductivity of thin SnO_x films allowed direct electrodeposition of active water oxidation electrocatalysts. The photocatalytic properties of electrodeposited catalysts have been

shown to be superior to compact pre-catalyst metal oxide films, as exemplified by electrodeposited NiFeOOH and sputter-deposited NiO_x.³¹ Electrodeposition allows high utilization of all of the elements in the deposited film, whereas compact films result in a substantial portion of the film that does not interact with the electrolyte. The high utilization of the film for catalysis results in a lower overpotential for the same optical transmission through the catalyst film. XPS indicates that the electrodeposited catalysts studied herein consist of oxides or hydroxides, with no apparent metallic peaks that would lead to parasitic light absorption. These properties allow planar photoanodes to be obtained with photocurrent densities under simulated sunlight of $\sim 30 \text{ mA cm}^{-2}$ and microcone array electrodes with photocurrent densities of 41-42 mA cm^{-2} .

3. *Properties of Atomic Layer Deposited SnO_x on Si microcones*

The conformal SnO_x coatings allow the construction of efficient three-dimensional photoanodes for water oxidation in both strongly acidic and strongly alkaline electrolytes. Although n-Si microcone arrays exhibit a lower efficiency than planar photoelectrodes, the study of microcone arrays is important to enable renewable energy technologies. Photoelectrochemical devices could benefit from the improved light trapping and flexibility of microstructured arrays, as well as the ability to use scalable semiconductor synthesis techniques such as vapor-liquid-solid growth.^{36,37} Structured semiconductors, such as Si microcone arrays, allow the decoupling of light-absorption paths and charge-transfer paths. This decoupling can allow defective semiconductors with short diffusion lengths to be used efficiently, because charge collection occurs at the sides of the high-aspect structure, whereas light absorption occurs throughout the length of the microcone. The high aspect-ratio tapered structure also minimizes reflection of incoming sunlight, which allows photocurrent densities of 41-42 mA cm^{-2} to be obtained with low loadings of catalyst, whereas planar samples exhibit photocurrent densities of 27-32 mA cm^{-2} (Table S1).⁶ Although

high aspect-ratio structures can improve the light-absorption properties, the open-circuit voltage (V_{oc}) of the device often decreases due to the increase in the diode saturation current resulting from the increase in junction area. The surface area of the microcone arrays studied herein is approximately 14.5 times higher than planar samples. The expected decrease in photovoltage is approximately 74 mV based on the ideality factor and diode current density measured on planar samples. A decrease of 110 – 130 mV was observed experimentally for n-Si microcone array electrodes compared to planar samples, indicating that the majority of the decrease can be attributed to the increase in junction area. The ~ 50 mV of photovoltage unaccounted for by the surface area increase could be due to non-optimal formation of the SiO_x layer during chemical oxidation; different junction properties for different surface terminations; or damage of the microcones during sample preparation. The overall decrease in photovoltage results in devices that are less efficient than planar samples. Further studies to address this issue could focus on developing junctions with substantially lower diode current densities, which could provide substantial improvements in photovoltage for high-surface area structures. Alternatively, transparent and insulating passivation layers could be used to reduce the junction area on high surface-area structures, which could also improve the photovoltage of such devices.

4. *Properties of $\text{SnO}_x/\text{TiO}_2$ Protective Bilayers*

The SnO_x layer formed an ohmic contact to TiO_2 , allowing the construction of $\text{SnO}_x/\text{TiO}_2$ bilayers that exhibited the rectifying properties of SnO_x and the protective properties of TiO_2 . Amorphous TiO_2 coatings have been used to protect n-Si, n-GaP, n-GaAs, and n-Si microwire arrays from corrosion or passivation in 1.0 M KOH(aq) for 100-2,200 h of continuous operation.^{11,}
³⁸ Although TiO_2 can protect various semiconductors for substantial periods of time, the band energetics at the n-Si/ TiO_2 interface lead to a relatively low photovoltage of ~ 360 mV under solar

illumination, with a diffused np^+ junction further increasing the photovoltage.¹¹ This behavior indicates that in $\text{SnO}_x/\text{TiO}_2$ bi-layers with a photovoltage of ~ 602 mV, the SnO_x layer has the effect of increasing the photovoltage compared to use only of TiO_2 . The SnO_x layers studied herein have favorable energetics for electron-hole pair separation and consequently lead to photovoltages of ~ 620 mV under solar illumination, but exhibit thermodynamic instability in alkaline environments. Figure S4 indicates that the SnO_x film exhibited slow but non-zero dissolution in corrosive electrolytes. The dissolution rate is substantially lower than previously reported for spray-deposited SnO_x protective films,¹² but the work reported herein primarily focuses on the alternative strategy of $\text{SnO}_x/\text{TiO}_2$ bilayers to obtain stable photoelectrodes. $\text{SnO}_x/\text{TiO}_2$ bilayers exhibited a similar photovoltage to SnO_x layers and an ohmic contact to each other, as indicated by the photovoltage and fill factor observed for n-Si/ $\text{SiO}_x/\text{SnO}_x/\text{TiO}_2/\text{Ni}$ photoanodes in contact with $\text{Fe}(\text{CN})_6^{3-/4-}(\text{aq})$ (Figure S12a). The work functions measured for SnO_x and TiO_2 indicate that negligible band-bending should occur at their interface (Figure S12b). The photoanodes coated with $\text{SnO}_x/\text{TiO}_2$ exhibited photocurrent stability for ~ 480 h, which is comparable to that observed in other systems protected with TiO_2 . The high photovoltage obtained for planar photoanodes protected by $\text{SnO}_x/\text{TiO}_2$ led to an ideal regenerative solar-to- $\text{O}_2(\text{g})$ efficiency of $\sim 3.5\%$. These results suggest that $\text{SnO}_x/\text{TiO}_2$ layers could be utilized for efficient and stable photoelectrochemical water-splitting devices in 1.0 M $\text{KOH}(\text{aq})$.

Conclusion

Conformal SnO_x coatings allowed the formation of three-dimensional heterojunctions that exhibited diode current densities of 1.3×10^{-11} A cm^{-2} , providing 620 mV and 490 mV of photovoltage on planar n-Si and n-Si microcone array electrodes, respectively. The SnO_x layer underwent an amorphous-to-crystalline transition after ~ 18 nm of growth, and band-bending at

the crystalline SnO_x/electrolyte junction had a strong influence on charge transfer to the electrolyte. The (photo)electrodeposition of OER catalysts such as NiFeOOH, CoO_x, and IrO_x on n-Si/SiO_x/SnO_x microcone arrays placed catalyst in regions that minimized parasitic light absorption, allowing light-limiting photocurrent densities of 41-42 mA cm⁻² under 100 mW cm⁻² of simulated solar illumination in 1.0 M KOH(aq) and 1.0M H₂SO₄(aq). Planar n-Si photoanodes coated with a bilayer of SnO_x and TiO₂ exhibited comparable efficiencies to that observed for photoanodes coated only with SnO_x, while exhibiting stability similar to photoanodes coated with TiO₂ in 1.0 M KOH(aq).

Experimental Section

Chemicals

All chemicals were used as received, including potassium ferrocyanide trihydrate (K₄Fe(CN)₆·3H₂O, Acros Organics, > 99%), potassium ferricyanide (K₃Fe(CN)₆, Fischer Scientific, Certified ACS), potassium chloride (KCl, Macron Chemicals, 99.6%), sulfuric acid (H₂SO₄, Fischer Scientific, TraceMetal Grade, 93-96%), potassium hydroxide (KOH, Sigma-Aldrich, Semiconductor Grade, 99.99%), hydrogen peroxide (H₂O₂, EMD Millipore Co., 30% aqueous solution), hydrochloric acid (HCl, EMD Millipore Co., 36-38% aqueous solution), potassium hexachloroiridate(IV) (K₂IrCl₆, Sigma-Aldrich, Technical Grade), nickel (II) nitrate hexahydrate (Ni(NO₃)₂·6H₂O, Sigma-Aldrich, 99.999%), iron(II) sulfate heptahydrate (FeSO₄·7H₂O, Sigma-Aldrich, ACS >99.0%), and gallium-indium eutectic (Alfa Aesar, 99.99%). A Barnsted Millipore system was used to obtain deionized water with 18.2 MΩ cm resistivity.

SiO_x Layer Formation

Silicon wafers were chemically oxidized by a procedure similar to previous reports.^{11, 12} Silicon polished in the (100) orientation having a degenerately doped p-type conductivity (p⁺-Si, $\rho < 0.005 \Omega \text{ cm}$) or n-type conductivity (n-Si, $\rho = 0.1\text{-}1 \Omega \text{ cm}$) was etched in a buffered oxide etch solution or HF(aq) for 1 min to remove the native silicon oxide layer, then rinsed with deionized water and dried under a flow of N₂(g). A controlled silicon oxide layer (SiO_x) was formed by placing the wafers in a 5:1:1 (v:v) H₂O/HCl/H₂O₂ solution at 75 °C for 10 min. The samples were then rinsed with deionized water and dried under N₂(g). Microcone arrays were treated with the same SiO_x growth process as planar samples to form a similar SiO_x layer.

Silicon Microcone Array Fabrication

Silicon wafers were coated with a 200 nm thick Al₂O₃ etch mask patterned using standard photolithography procedures into an array of 3 μm diameter circles with 7 μm pitch. The microcone arrays were etched in an Oxford Dielectric System 100 ICP/RIE. The etching procedure was similar to a previous report.⁶ The etch was performed at a capacitive coupled power of 7 W and an inductively coupled power of 900 W. The etch was performed in three 30 min steps consisting of 70 sccm of SF₆ with an O₂ flow rate of 6.0, 6.5, and 7.0 sccm, respectively. The chamber temperature and pressure were maintained at -130 °C and 10 mTorr, respectively.

Sample Preparation

Atomic-layer deposition (ALD) was performed with a Cambridge Nanotech S200 ALD system. Tin oxide (SnO_x) films were deposited with alternating pulses of (tetrakis-dimethylamino)tin(IV) (TDMASn, Strem Chemicals, 99.99% Sn) and ozone (O₃). An ALD cycle consisted of a 0.3 s pulse of TDMASn, a 20 s purge under 20 sccm flow of N₂(g), a 0.1 s pulse of O₃, and a 30 s purge under 20 sccm flow of N₂(g). The samples were held at 210 °C during the

SnO_x deposition unless otherwise specified. Titanium dioxide (TiO₂) films were deposited with a previously reported procedure.¹¹ An ALD TiO₂ deposition cycle consisted of a 0.1 s pulse of tetrakis-dimethylamidotitanium (TDMAT, Sigma-Aldrich), a 15 s purge under 20 sccm flow of N₂(g), a 0.015 s pulse of H₂O, and a 15 s purge under 20 sccm flow of N₂(g). The samples were held at 150 °C during the TiO₂ deposition. The TDMASn and TDMAT ALD cylinders were held at 60 °C and 75 °C with heating jackets.

An AJA Orion sputtering system was used to deposit metallic films of Ni or Pt. The films were sputtered from an Ar plasma with Ni (ACI Alloys) or Pt (ACI Alloys) metal targets. The chamber pressure was < 10⁻⁷ Torr prior to sputter deposition. The Ar plasma was maintained during the deposition at a chamber pressure of 5 mTorr with an Ar flow rate of 20 sccm. The Ni and Pt films were deposited with a RF target power of 150 W and 150 W, respectively. Deposition rates were calibrated with ~ 100 nm thick films via profilometry (DektakXT Stylus profilometry) measurements. The duration of the sputtering was used to control the thickness of the metal films, and the samples were not intentionally heated during the deposition.

Electrodes were prepared with methods similar to previous work.^{11, 12} Si wafers were cleaved into ~ 0.25 cm² pieces, and ohmic contacts were made by either scribing In-Ga eutectic (Aldrich) on the back or thermally evaporating 50-100 nm of Al on the back prior to ALD depositions with an AJA Orion system equipped with a thermal evaporator. Tinned Cu wire was threaded through glass tubes, and Ag paint (SPI, Inc.) was used to make an electrical contact between the sample and the Cu wire as well as to provide mechanical stability to the contact. The contact was dried for at least 2 h at room temperature. Epoxy (Hysol 9460) was used to insulate the back contact and to define the electrode area. The epoxy was cured for at least 12 h at room temperature prior to use. Electrode areas were determined by using an optical scanner (Epson

perfection V360) to image the electrodes and ImageJ software to process the images. The electrode areas were between 5 and 20 mm² unless otherwise specified.

Acknowledgements

This work was supported through the Office of Science of the U.S. Department of Energy (DOE) under award no. DE-SC0004993 to the Joint Center for Artificial Photosynthesis, a DOE Energy Innovation Hub, and in part by the National Science Foundation (NSF) and the Department of Energy (DOE) under NSF CA No. EEC-1041895. Any opinions, findings and conclusions or recommendations expressed in this material are those of the author(s) and do not necessarily reflect those of NSF or DOE. Fabrication was performed in Kavli Nanoscience Institute (KNI) at Caltech, and we thank KNI staff for their assistance during fabrication. I.M.H acknowledges a National Science Foundation Graduate Research Fellowship under Grant No. DGE-1144469. We thank C. Garland for assistance with transmission-electron microscopy measurements.

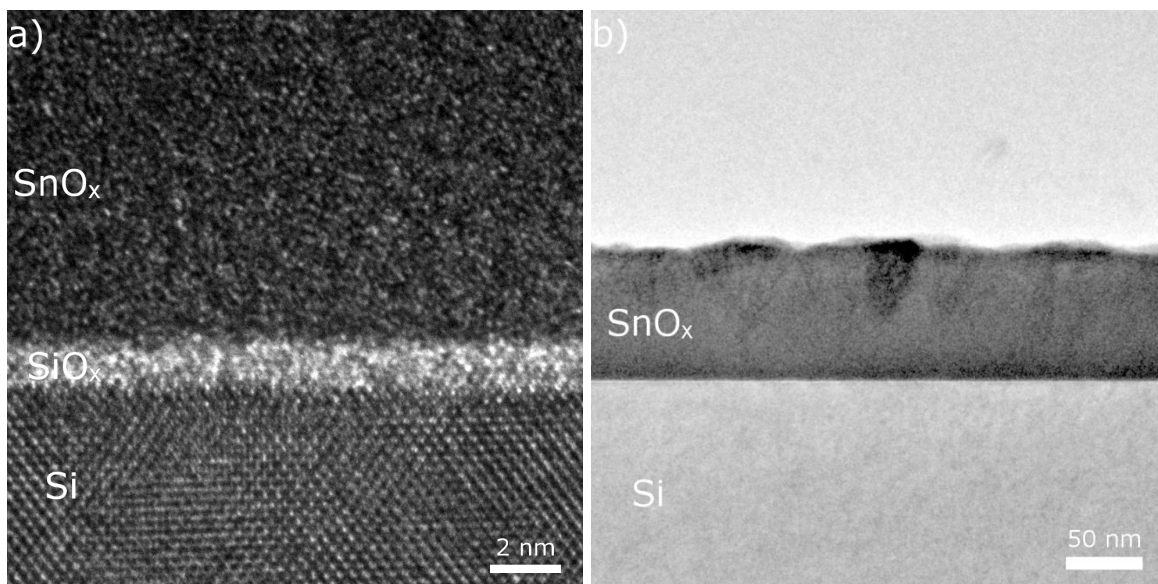
Figures:

Figure 1. a) High-resolution transmission-electron microscopy (HRTEM) of the n-Si/SiO_x/SnO_x interface. b) Transmission-electron microscopy image of n-Si/SiO_x/SnO_x cross-section.

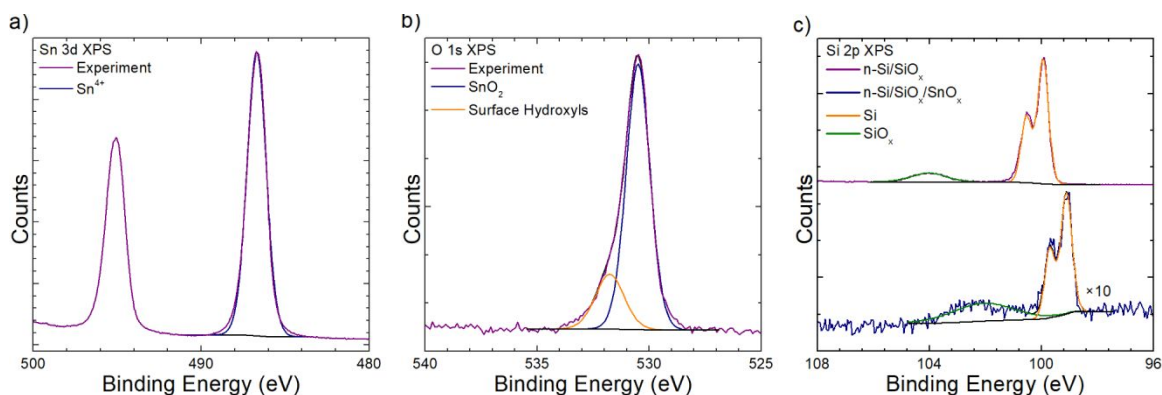


Figure 2. Chemical characterization of SnO_x film. a) High-resolution XP spectra in the Sn 3d region of SnO_x deposited at 210 °C with 850 ALD cycles on a quartz substrate. b) High-resolution XP spectra in the O 1s region of SnO_x deposited at 210 °C with 850 ALD cycles on a quartz substrate. High-resolution XP spectra in the Si 2p region of n-Si/SiO_x, and n-Si/SiO_x/SnO_x of SnO_x deposited at 210 °C with 50 cycles on an n-Si/SiO_x substrate.

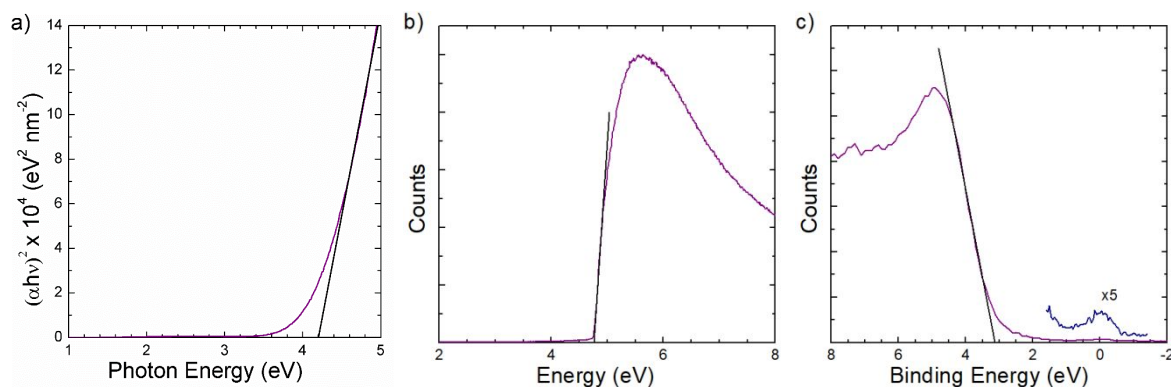


Figure 3. UV-Vis and XPS measurements of SnO_x deposited at 210°C with 850 ALD cycles on a quartz substrate. a) Direct band gap determined by the Tauc plot method from transmission UV-Vis spectroscopy measurements. b) Fermi-level position determined from the secondary-electron energy cut-off of a sample under bias within an XPS instrument. c) Valence-band spectrum of SnO_x .

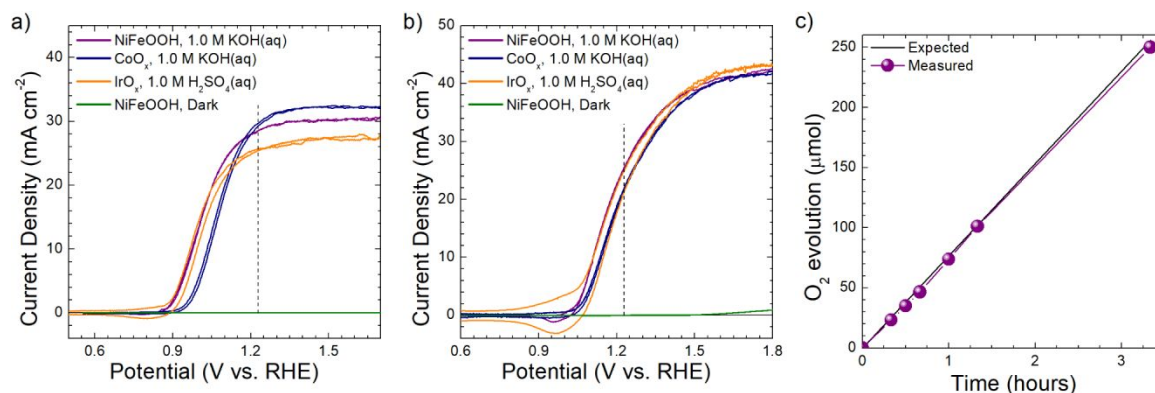


Figure 4. a) Photoelectrochemical behavior of n-Si/ SiO_x photoanodes coated with 100 cycles of SnO_x and electrodeposited water-oxidation catalysts. b) Photoelectrochemical behavior of n-Si microcone arrays coated with 100 cycles of SnO_x and electrodeposited water-oxidation catalysts. c) Comparison between measured oxygen and oxygen expected from 100% faradaic efficiency for

water-oxidation for an n-Si/SiO_x planar photoanode coated with SnO_x/Ni under simulated solar illumination as measured with an eudiometer.

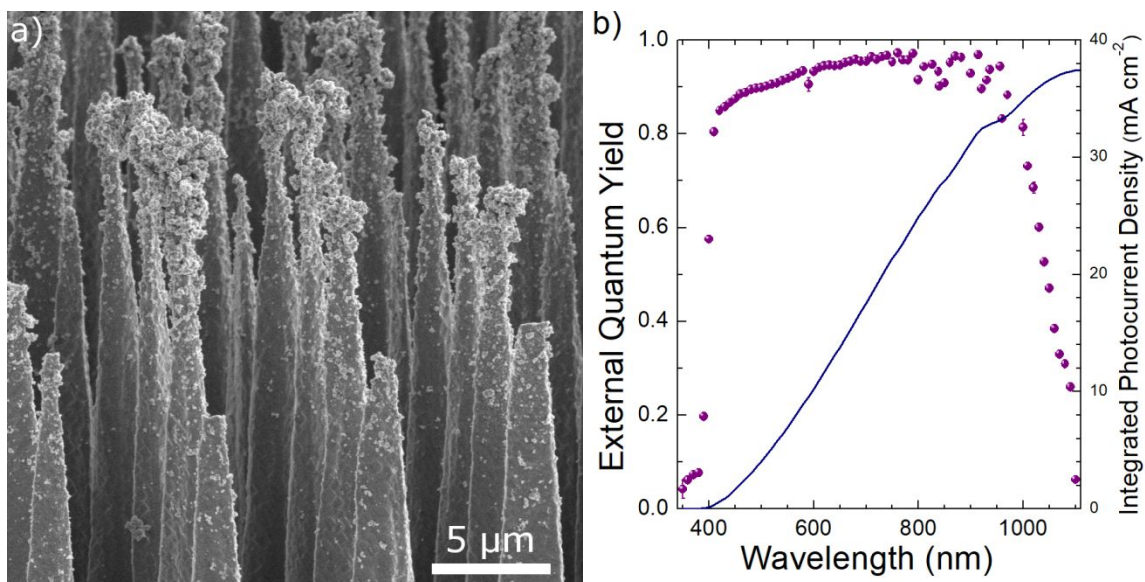


Figure 5. a) SEM image of n-Si microcones coated with 100 cycles of SnO_x and an electrodeposited IrO_x catalyst. b) External quantum yield at 1.506 V vs. RHE of n-Si microwire arrays coated with 100 cycles of SnO_x and an electrodeposited CoO_x catalyst, and expected photocurrent density obtained by integrating the product of the spectral photon flux of the AM 1.5G spectrum and the external quantum yield at each wavelength.

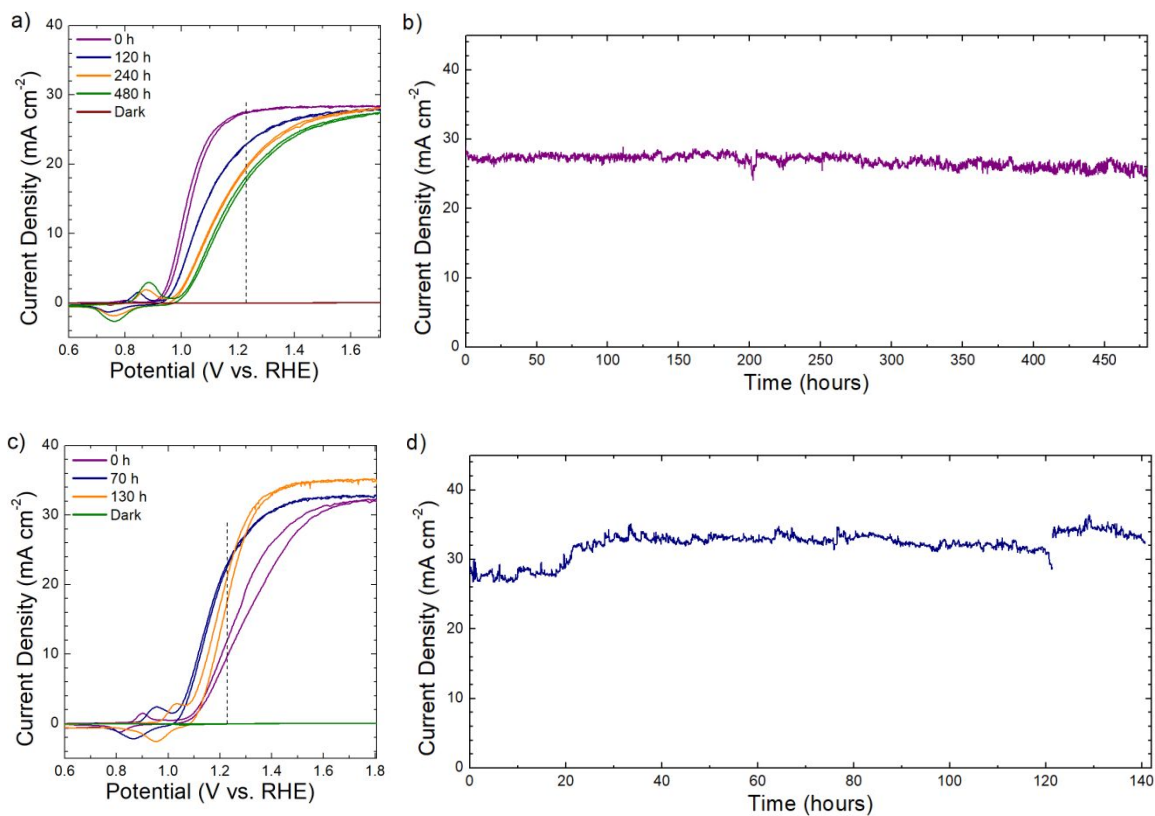


Figure 6. Photoelectrochemical behavior of n-Si/SiO_x photoanodes coated with SnO_x/TiO₂ and Ni in contact with 1.0 M KOH(aq) under 100 mW cm⁻² of simulated solar illumination. a) Cyclic voltammetry from 0.6 V to 1.706 V vs. RHE of planar n-Si with SnO_x/TiO₂ and 3.5 nm of Ni. b) Photocurrent stability of planar n-Si photoanodes with SnO_x/TiO₂ and 3.5 nm of Ni at 1.606 V vs. RHE. c) Cyclic voltammetry from 0.6 V to 1.806 V vs. RHE of n-Si microcone array photoanodes coated with SnO_x/TiO₂ and 7 nm of Ni. d) Photocurrent stability of n-Si microcone array photoanodes coated with SnO_x/TiO₂ and 7 nm of Ni at 1.806 V vs. RHE.

References

1. E. L. Warren, H. A. Atwater and N. S. Lewis, *J. Phys. Chem. C*, 2013, **118**, 747-759.
2. N. S. Lewis, *Nat. Nanotech.*, 2016, **11**, 1010-1019.
3. I. Narkeviciute, P. Chakthranont, A. J. Mackus, C. Hahn, B. A. Pinaud, S. F. Bent and T. F. Jaramillo, *Nano Lett.*, 2016, **16**, 7565-7572.
4. M. R. Shaner, K. T. Fountaine, S. Ardo, R. H. Coridan, H. A. Atwater and N. S. Lewis, *Energy Environ. Sci.*, 2014, **7**, 779-790.
5. P. Chakthranont, T. R. Hellstern, J. M. McEnaney and T. F. Jaramillo, *Adv. Energy Mater.*, 2017, **7**.
6. S. Yalamanchili, H. S. Emmer, K. T. Fountaine, C. T. Chen, N. S. Lewis and H. A. Atwater, *ACS Photonics*, 2016, **3**, 1854-1861.
7. M. Dasog, A. I. Carim, S. Yalamanchili, H. A. Atwater and N. S. Lewis, *Nano Lett.*, 2016, **16**, 5015-5021.
8. N. S. Lewis, *Science*, 2016, **351**, aad1920.
9. D. Bae, B. Seger, P. C. Vesborg, O. Hansen and I. Chorkendorff, *Chem. Soc. Rev.*, 2017, **46**, 1933-1954.
10. M. F. Lichterman, K. Sun, S. Hu, X. Zhou, M. T. McDowell, M. R. Shaner, M. H. Richter, E. J. Crumlin, A. I. Carim, F. H. Saadi, B. S. Brunshwig and N. S. Lewis, *Catal. Today*, 2016, **262**, 11-23.
11. S. Hu, M. R. Shaner, J. A. Beardslee, M. Lichterman, B. S. Brunshwig and N. S. Lewis, *Science*, 2014, **344**, 1005-1009.
12. I. A. Moreno-Hernandez, B. S. Brunshwig and N. S. Lewis, *Adv. Energy Mater.*, 2018, **8**, 1801155.
13. Y. W. Chen, J. D. Prange, S. Duhnen, Y. Park, M. Gunji, C. E. Chidsey and P. C. McIntyre, *Nat. Mater.*, 2011, **10**, 539-544.
14. J. Yang, K. Walczak, E. Anzenberg, F. M. Toma, G. Yuan, J. Beeman, A. Schwartzberg, Y. Lin, M. Hettick, A. Javey, J. W. Ager, J. Yano, H. Frei and I. D. Sharp, *J. Am. Chem. Soc.*, 2014, **136**, 6191-6194.
15. T. Yao, R. Chen, J. Li, J. Han, W. Qin, H. Wang, J. Shi, F. Fan and C. Li, *J. Am. Chem. Soc.*, 2016, **138**, 13664-13672.

16. B. Mei, T. Pedersen, P. Malacrida, D. Bae, R. Frydendal, O. Hansen, P. C. K. Vesborg, B. Seger and I. Chorkendorff, *J. Phys. Chem. C*, 2015, **119**, 15019-15027.
17. M. J. Kenney, M. Gong, Y. Li, J. Z. Wu, J. Feng, M. Lanza and H. Dai, *Science*, 2013, **342**, 836-840.
18. Y. Yu, Z. Zhang, X. Yin, A. Kvit, Q. Liao, Z. Kang, X. Yan, Y. Zhang and X. Wang, *Nat. Energy*, 2017, **2**.
19. A. Azarpira, T. Schedel-Niedrig, H. J. Lewerenz and M. Lublow, *Adv. Energy Mater.*, 2016, **6**, 1502314.
20. L. Ji, H. Y. Hsu, X. Li, K. Huang, Y. Zhang, J. C. Lee, A. J. Bard and E. T. Yu, *Nat. Mater.*, 2017, **16**, 127-131.
21. A. G. Scheuermann, J. P. Lawrence, K. W. Kemp, T. Ito, A. Walsh, C. E. Chidsey, P. K. Hurley and P. C. McIntyre, *Nat. Mater.*, 2016, **15**, 99-105.
22. L. Chen, J. Yang, S. Klaus, L. J. Lee, R. Woods-Robinson, J. Ma, Y. Lum, J. K. Cooper, F. M. Toma, L. W. Wang, I. D. Sharp, A. T. Bell and J. W. Ager, *J. Am. Chem. Soc.*, 2015, **137**, 9595-9603.
23. O. L. Hendricks, R. Tang-Kong, A. S. Babadi, P. C. McIntyre and C. E. D. Chidsey, *Chem. Mater.*, 2018, **31**, 90-100.
24. Z. Luo, T. Wang and J. Gong, *Chem. Soc. Rev.*, 2019, **48**, 2158-2181.
25. W. Yang, R. R. Prabhakar, J. Tan, S. D. Tilley and J. Moon, *Chem. Soc. Rev.*, 2019, **48**, 4979-5015.
26. R. H. Coridan, A. C. Nielander, S. A. Francis, M. T. McDowell, V. Dix, S. M. Chatman and N. S. Lewis, *Energy Environ. Sci.*, 2015, **8**, 2886-2901.
27. D.-w. Choi and J.-S. Park, *Surf. Coat. Technol.*, 2014, **259**, 238-243.
28. M. A. Stranick and A. Moskwa, *Surf. Sci. Spectra*, 1993, **2**, 45-49.
29. M. A. Stranick and A. Moskwa, *Surf. Sci. Spectra*, 1993, **2**, 50-54.
30. S. Hu, M. H. Richter, M. F. Lichterman, J. Beardslee, T. Mayer, B. S. Brunschwig and N. S. Lewis, *J. Phys. Chem. C*, 2016, **120**, 3117-3129.
31. K. Sun, I. A. Moreno-Hernandez, W. C. Schmidt, X. Zhou, J. C. Crompton, R. Liu, F. H. Saadi, Y. Chen, K. M. Papadantonakis and N. S. Lewis, *Energy Environ. Sci.*, 2017, **10**, 987-1002.

32. Y. Zhao, N. M. Vargas-Barbosa, E. A. Hernandez-Pagan and T. E. Mallouk, *Small*, 2011, **7**, 2087-2093.
33. L. Trotochaud, S. L. Young, J. K. Ranney and S. W. Boettcher, *J. Am. Chem. Soc.*, 2014, **136**, 6744-6753.
34. S. J. Freakley, J. Ruiz-Esquiús and D. J. Morgan, *Surf. Interface Anal.*, 2017, **49**, 794–799.
35. P. K. Nayak, J. Bisquert and D. Cahen, *Adv. Mater.*, 2011, **23**, 2870-2876.
36. S. W. Boettcher, J. M. Spurgeon, M. C. Putnam, E. L. Warren, D. B. Turner-Evans, M. D. Kelzenberg, J. R. Maiolo, H. A. Atwater and N. S. Lewis, *Science*, 2010, **327**, 185-187.
37. M. D. Kelzenberg, S. W. Boettcher, J. A. Petykiewicz, D. B. Turner-Evans, M. C. Putnam, E. L. Warren, J. M. Spurgeon, R. M. Briggs, N. S. Lewis and H. A. Atwater, *Nat. Mater.*, 2010, **9**, 239-244.
38. M. R. Shaner, S. Hu, K. Sun and N. S. Lewis, *Energy Environ. Sci.*, 2015, **8**, 203-207.

